




Deformation behavior of crystalline/amorphous Al-Si nanocomposites with nanolaminate or nanofibrous microstructures

Bibhu Prasad Sahu ^{1,*}, Wenqian Wu,³ Jian Wang,³ and Amit Misra ^{1,2,†}

¹Department of Materials Science and Engineering, University of Michigan, Ann Arbor, Michigan 48109, USA

²Department of Mechanical Engineering, University of Michigan, Ann Arbor, Michigan 48109, USA

³Mechanical and Materials Engineering, University of Nebraska-Lincoln, Lincoln, Nebraska 68588, USA

 (Received 1 June 2022; revised 22 August 2022; accepted 24 August 2022; published 7 September 2022)

Deformation mechanisms in sputter-deposited crystalline Al/amorphous Si nanocomposites with nanolaminate or nanofibrous morphology are characterized by nanoindentation, micropillar compression testing and transmission electron microscopy (TEM). The nanofibrous composite having crystalline Al nanofibers with ~ 40 – 50 nm in length and 15 – 20 nm in diameter embedded in amorphous Si exhibits strain hardening to a maximum flow stress of 2.9 GPa and no shear band (SB) formation in compression up to plastic strain exceeding 24% . On the other hand, nanolaminate composite that is composed of 80 nm crystalline Al layers and 20 nm amorphous Si layers exhibits catastrophic SBs starting at plastic strains in the range of 5 – 10% . Cross-sectional TEM of the deformed samples reveals a high density of stacking faults and twin boundaries in Al nanofibers and no microshear bands in the nanofibrous composite, suggesting plastic deformation in amorphous Si phase and crystalline Al nanofibers. Molecular dynamics simulations revealed that the plastic deformation in amorphous Si phase in the cosputtered films could be favored by the decrease in flow strength of amorphous Si with increasing Al solute concentration trapped in Si.

DOI: [10.1103/PhysRevMaterials.6.094002](https://doi.org/10.1103/PhysRevMaterials.6.094002)

I. INTRODUCTION

Crystalline-amorphous composites exhibit great potential to achieve high strength and improved ductility through manipulation of the microstructural length scales, morphology, and chemistry [1]. In the case of crystalline/metallic glass laminates, a tendency to suppress shear bands (SBs) was reported for nanolaminates with (i) bilayer period $< \approx 100$ nm, and (ii) within a bilayer, the glassy layer being significantly thinner than the crystalline layer, in Cu-Cu(Zr) [2–6], Cu-Pd(Si) [7,8], Cu-Cu(Nb) [9,10], and other [11,12] systems. The interfaces of crystal/amorphous (C/A) nanolaminates are different from that of crystal/crystal (C/C) interfaces and grain boundaries due to the absence of specific crystallographic orientations as well as relatively low interface energy [3]. The tendency to suppress catastrophic SBs in C/A nanolaminates is attributed to the mutual elastic and plastic constraints at the C/A interface [13,14] and the intrinsic small-scale size effects in glass [15].

In addition to nanolaminates, other microstructures in C/A nanocomposites have also attracted interest [16–20]. For example, amorphous intergranular films at grain boundaries in nanocrystalline Cu-Zr alloys were shown to mitigate radiation damage [16]. Uniform distribution of Zr(Mo) nanocrystallites in an amorphous Zr-rich matrix in sputter-deposited thin film of $Zr_{1-x}Mo_x$ alloy exhibited higher hardness than the bulk Zr and Mo [17]. Ming *et al.* [1] demonstrated that three-

dimensional, bicontinuous C/A nanoarchitectures of a TiZr-based alloy exhibited enhanced ductility and strain hardening capability compared with both amorphous and crystalline phases. However, the role of the microstructural morphology, e.g., fibrous vs laminate, of the constituent phases in the C/A nanocomposites in influencing the flow strength, strain hardening, and SB formation is not understood.

In this paper, the nanomechanical behavior of C/A Al-Si nanocomposites involving crystalline Al and covalently bonded Si amorphous phases for two different microstructures, nanolaminate and nanofibrous, is reported. Crystalline Al 80 nm/amorphous 20 nm nanolaminates are synthesized by sequential sputtering. Earlier literature has shown that it could be possible to achieve phase-separated nanocrystalline Al columnar grains embedded in amorphous Si matrix through either magnetron cosputtering [21,22] or electron beam co-evaporation [23], although mechanical behavior was not reported. Here, we grow crystalline Al nanofibers in a matrix of amorphous Si via cosputtering Al 63 at. % and Si 37 at. %. Further, it is important to note that the deformation mechanism in amorphous Si is expected to be different from that of other metallic glass systems because of the fundamental difference in atomic bonding [21,22]. The covalent Si-Si bonds are generally strong, highly directional, and resistant to plastic deformation [24]. Recent studies on laser rapid solidified Al-(16 – 20) wt. % Si alloys have shown significant increases in both tensile strength and ductility as compared with arc-melted Al-Si alloys [25], but these alloys only involved C/C phases. Using nanoindentation, micropillar compression testing, and transmission electron microscopy (TEM), the deformation mechanisms of the layered and

*bpsahu@umich.edu, bibhu.igit@gmail.com

†amitmis@umich.edu

fibrous morphologies of crystalline Al/amorphous Si composite thin films are characterized. Molecular dynamics (MD) simulation (see Sec. S1 in the Supplemental Material [26] for computational details) was used to model the flow strength of amorphous Si with varying levels of trapped Al solute atoms.

II. EXPERIMENTAL PROCEDURES

A. Material synthesis

The Al-Si thin films were physically vapor-deposited on thermally oxidized Si substrates of dimension 10×10 mm at room temperature using direct current magnetron sputtering (model: Kurt J Lesker PVD 75) with high-purity (99.99%) elemental targets of Al and Si at 100 and 60 W, respectively. To avoid the substrate heating, water cooling was continued throughout the deposition process. Before deposition, the substrates were precleaned by applying a 20 W bias on the substrate for 10 min. To maintain a uniform deposition, the substrates were rotated at 10 rpm. For the film with nanolaminate structure, sequential deposition of the Al and Si layers was carried out, whereas a cosputtering condition was used for the deposition of the film with fibrous morphology. The base pressure of the sputtering chamber was set at 1.07×10^{-5} Pa with a working pressure of 0.39 Pa of argon. The total film thickness was $2 \mu\text{m}$, and the deposition rates for Al and Si were 1.22 and 0.45 nm/s, respectively, for both types of films.

B. Mechanical tests

The indentation hardness of the films was measured with a standard Berkovich indenter tip in conjunction with a load- and depth-sensing nanoindenter system (Bruker TI 950 Triboindenter). The hardness tests were conducted by making 12 nanoindents on the sample under a load-control cycle, which increased the load linearly with time during each indent, from 0 to a specified maximum value of 5 mN at a loading rate of 0.2 mN/s. The total indentation depth was limited to $\leq 10\%$ of the total film thickness to avoid the substrate effect. Micropillar compression tests with a pillar dimension of $1 \mu\text{m}$ diameter \times $2 \mu\text{m}$ height were carried out with a flat-tipped punch with tip diameter of $\sim 10 \mu\text{m}$ to measure the stress-strain behavior. The indenter was pressed against the films at an initial strain rate of $1 \times 10^{-4} \text{ s}^{-1}$, and tests were conducted to a nominal strain of $\approx 25\%$ (maximum displacement of 500 nm). The stress-strain curves were determined according to load-displacement data, which were continuously recorded during the micropillar compression tests. A homogeneous deformation assumption model with constant volume was used during analysis of the load-displacement data. The used model system was successfully applied in previous studies [27–29]. For a micropillar consisting of thin film and substrate, the total displacement can be decomposed into two components: (i) the length change in film and (ii) the elastic displacement in the micropillar base caused by Sneddon's effect, where the effect of the substrate is considered [30]. Given the loading force P and displacement u , the length change in film Δl_f can be calculated as

$$\Delta l_f = u - (P \times C_{\text{Sneddon}}), \quad (1)$$

in which

$$C_s = \frac{l_s}{E_s \times A_s}, \quad (2)$$

$$C_{\text{Sneddon}} = \frac{(1 - \nu_s^2)}{2E_s} \sqrt{\frac{\pi}{A_{\text{bottom}}}}, \quad (3)$$

where E_s is the elastic modulus, and ν_s is Poisson's ratio of the Si substrate, respectively, while l_s is its length, and the area at the bottom of the micropillars (where Si acts as the base of the micropillars) is A_{bottom} . Here, C_s is the compliance of the substrate part of the micropillar, while C_{Sneddon} considers Sneddon's effect. Finally, Δl_f has been used to calculate the engineering strain, whereas the initial cross-sectional area of the film part was considered to calculate the engineering stress. Further, tapering of the micropillar has been considered during estimating the engineering stress value of the films after incorporating the correction factor. (Detailed description of the effect of the tapering and the correction factor used to modify the uncorrected stress value of the micropillars is described in Sec. S2 in the Supplemental Material [26].)

C. Microstructural characterization

The microstructures of the as-deposited films before and after deformation were imaged by scanning electron microscopy (SEM). Cylindrical micropillars with a diameter of $1 \mu\text{m}$ and $2 \mu\text{m}$ in height were fabricated using a dual-beam focused ion beam (FIB) system (Helios 650 Nanolab) operated at a final beam current of 60 pA and a constant accelerating voltage of 30 kV. Further, the microstructural characterization of the as-deposited and deformed films was conducted using TEM (Thermo Fisher Talos F200X G2) S/TEM operated at 200 kV. The TEM specimens were prepared by FIB in a Helios 650 Nanolab SEM by the lift-out technique.

III. RESULTS

A. Microstructures of Al-Si nanolaminates

Figure 1(a) shows the TEM bright-field (BF) image of FIB-prepared cross-sections of the nanocrystalline Al/amorphous Si multilayers. The low-magnification BF image depicts the continuous layers of Al and Si arranged in an alternate fashion [Fig. 1(a)]. The red arrow marks the film growth direction. The total thickness of the multilayer film measured from Fig. 1(a) is found to be $2 \pm 0.04 \mu\text{m}$. The individual layer thickness was measured to be ~ 80 nm for Al layers and 20 nm for Si layers. The difference in contrast of the Al layers reveals an in-plane grain width of 40 ± 3 nm. Numerous Al grains have been considered to estimate the average value. Figure 1(b) depicts the selected area diffraction (SAD) pattern of the location denoted by the dotted square in Fig. 1(a), which represents the diffraction rings of the nanocrystalline Al layers with a weak $\{111\}$ Al fiber texture along the growth direction. The elemental mapping analysis of the designated location of Fig. 1(a) is shown in Fig. 1(c), showing the distribution of Al and Si. The high-resolution scanning TEM (HRSTEM) of the film focusing on one layer of Al and Si is shown in Fig. 1(d), revealing the interface between crystalline Al and amorphous Si. The contrast from the Si layer appears to be featureless, consistent with amorphous structure. The fast Fourier trans-

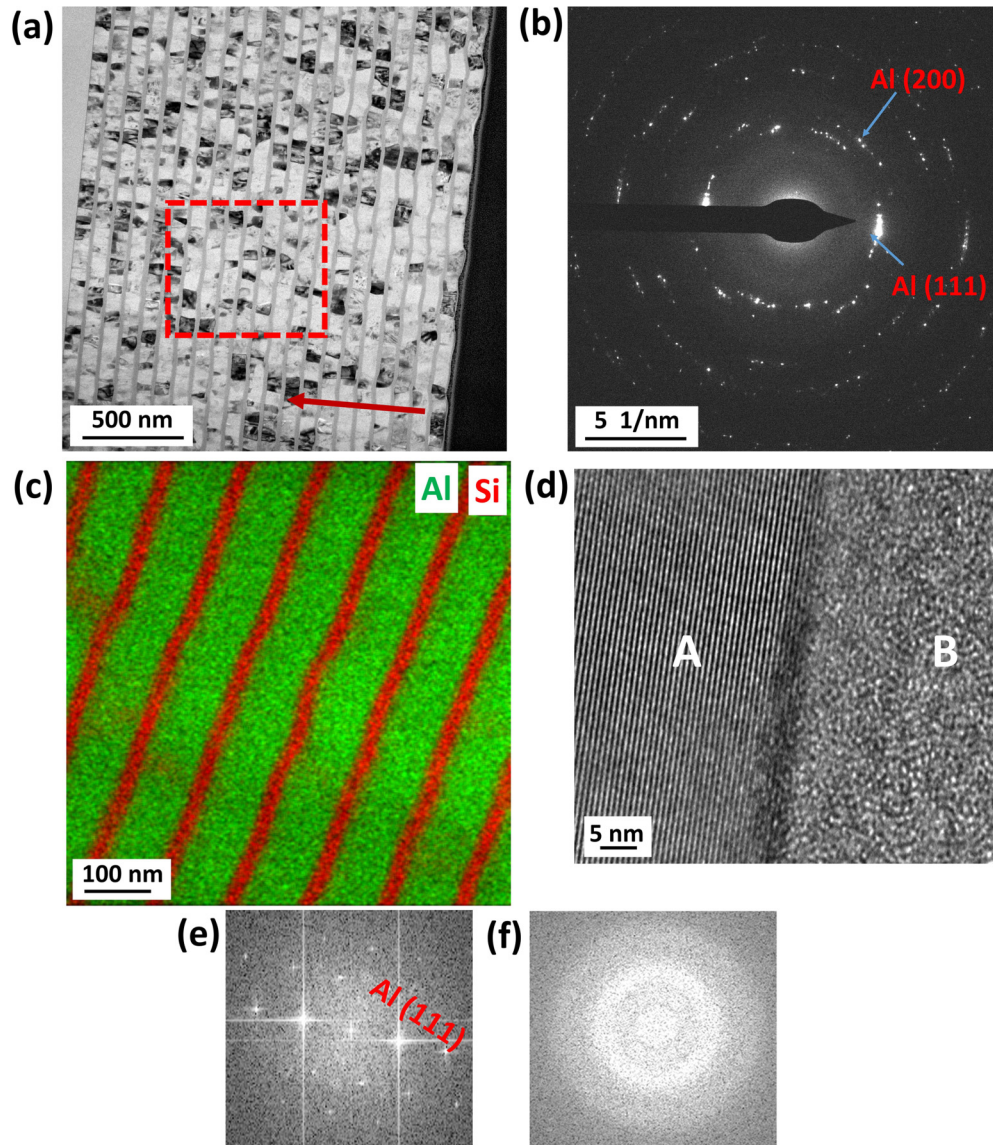


FIG. 1. Microstructure of focused ion beam (FIB)-prepared cross-sectional lamellae of the multilayer film. (a) Transmission electron microscopy (TEM) bright-field image. (b) Selected area electron diffraction (SAED) pattern of the highlighted portion. (c) Elemental scanning TEM (STEM) mapping showing alternating layers of Al and Si. (d) High-resolution STEM (HRSTEM) BF image highlighting the crystalline Al and amorphous Si layer. (e) Fast Fourier transform (FFT) pattern of the crystalline Al layer from the marked region A. (f) FFT pattern of the amorphous Si layer from the marked region B.

form (FFT) of regions A and B marked in Fig. 1(d) confirms the crystalline structure of the Al layers [Fig. 1(e)] and the amorphous structure of the Si layers [Fig. 1(f)], respectively.

B. Microstructure of the cosputtered Al-Si film

The cosputtered Al-Si film undergoes a transition in microstructure from very fine nanograins of Al distributed randomly in the amorphous Si-rich matrix to nanofibers of Al with increasing film thickness [Fig. 2(a)]. The arrow in Fig. 2(a) identifies the film growth direction. Figure 2(b) depicts the SAD pattern taken from region A, showing numerous continuous rings arising from nanocrystalline Al grains with a diffuse halo of the amorphous Si-rich phase. The overall elemental composition of the cosputtered film obtained using STEM energy dispersive x-ray spectroscopy is ~ 63

± 1.5 at. % Al and $\sim 37 \pm 1.0$ at. % Si. The average value of the elemental composition was estimated by considering several regions in the microstructure with TEAM software. The elemental STEM mapping showing the distribution of Al and Si close to the substrate surface is shown in the Supplemental Material (see Fig. S3 in Sec. S3) [26], indicating the homogeneous distribution of fine clusters of Al in Si matrix. The average volume fraction of the phases estimated from the mapping considering several locations suggests that Al and Si phases belong to $\sim 65 \pm 7$ vol. % and $\sim 35 \pm 7$ vol. %, respectively. However, Fig. 2(c) represents the diffraction pattern from region B, with more distinct rings of Al nanocrystalline grains, such as (111), (220), and (200) planes, which confirms coarsening of the in-plane dimension of the Al crystallites with increasing film thickness. Further, Fig. 2(d) demonstrates the magnified BF STEM image from location

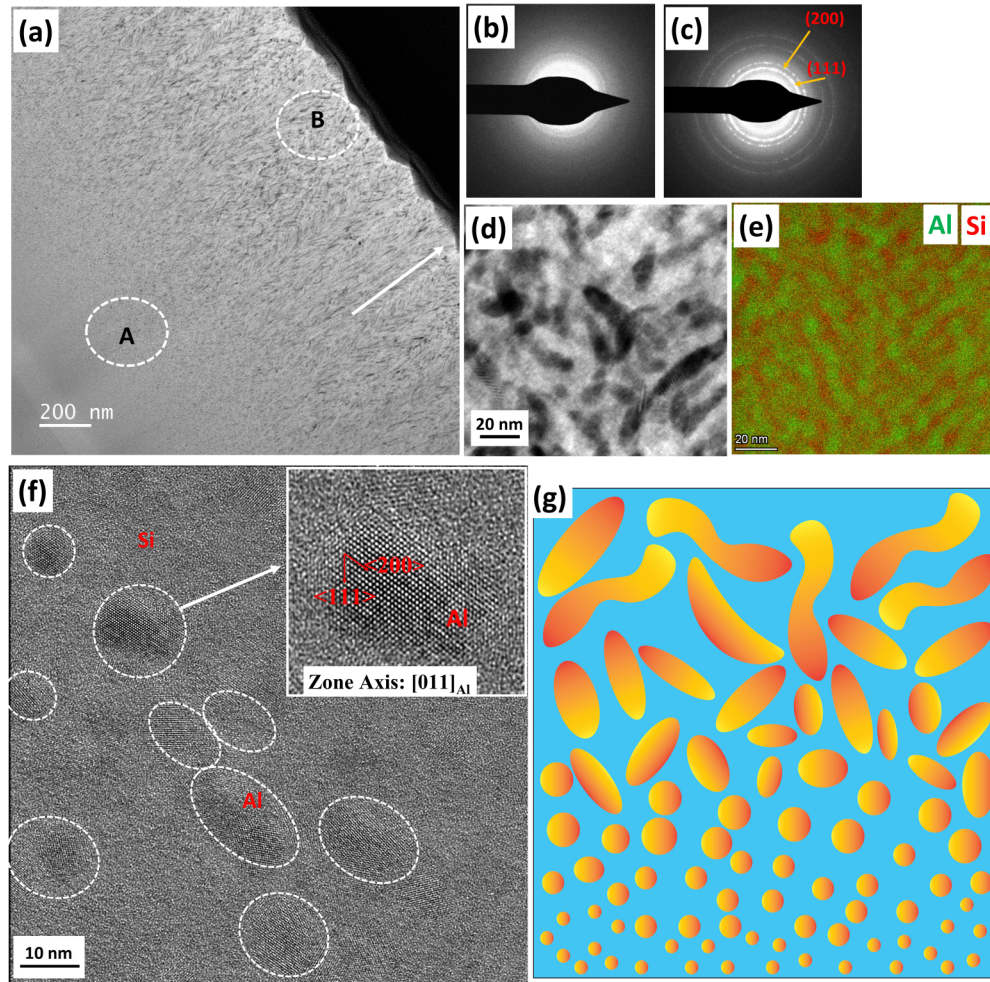


FIG. 2. Microstructures of the nanofibrous Al-Si film. (a) Low-magnification transmission electron microscopy (TEM) bright-field (BF) image. (b) Selected area diffraction (SAD) pattern from region A. (c) SAD pattern from region B. (d) Enlarged scanning TEM (STEM) BF near the surface showing the nanofibers of Al. (e) Elemental STEM mapping showing the distribution of Al and Si. (f) High-resolution STEM BF image of the film near the substrate showing the nanograins of Al embedded in amorphous Si matrix. The inset shows the magnified version of one Al grain showing different plane direction in $[011]_{\text{Al}}$ zone axis. (g) Schematic representation of the growth of the Al fiber in Si matrix.

B, which indicates the uniform distribution of the Al grains having elongated fiber morphology (length $\approx 40\text{--}50$ nm, width $\approx 15\text{--}20$ nm) with a spacing of ~ 20 nm in the amorphous Si matrix. The elemental STEM mapping of location A indicates the distribution of the elemental Al (green) in the fiber morphology dispersed in the Si phase (red). The volume fraction of the phases is estimated to be $\sim 67 \pm 4$ vol.% of Al and $\sim 33 \pm 4$ vol.% of Si. A high-resolution STEM (HRSTEM) BF micrograph of the location selected close to the substrate confirms the random distribution of the Al grains embedded in the amorphous Si matrix [Fig. 2(f)]. For a clear view, the magnified image of one of the Al nanograins is shown in the inset of Fig. 2(f) indicating directions of different planes of Al in $[011]$ beam direction. A schematic representation of the growth of the Al nanofibers embedded in the amorphous Si matrix is depicted in Fig. 2(g). By considering the variation in microstructure of the fibrous film, the schematic interpretation [Fig. 2(g)] suggests that, as the deposition starts from the substrate surface, dual amorphous structures (rich in Si) are possible, consistent with a microstructure which reveals the formation of disordered crystalline Al nanograins nucleated

randomly in the amorphous matrix. Further, the continued codeposition along the thickness direction leads to formation of an ordered crystalline Al phase with increasing size, finally transforming into a fiber-shaped structure separated from the amorphous Si matrix.

C. Nanoindentation behavior

Under a maximum load of 5 mN, the indentation hardness of the Al-Si multilayer was measured to be 4.1 ± 0.39 GPa (Table I), which is almost twice the indentation hardness of the magnetron sputtered pure Al film, as reported by Barajas-Valdes and Suárez [31]. Figures 3(a) and 3(b) show a series of TEM micrographs with increasing magnifications revealing the indent impression. A representative plan-view SEM image of the indentation mark was shown in Fig. 3(a) as the inset. The projected contact area of the indented mark is depicted in Fig. 3(b). Careful examination of the cross-sections through the indentation reveals the preferential thinning of the Al layers beneath the tip as well as large plastic strains near the indent [Fig. 3(b)]. The elemental

TABLE I. The measured values of hardness (H), compressive flow strength (σ_{flow}), critical stress required for activation of SBs (σ_{pro}) using Eq. (4), incubation length scale (h_{inc}) using Eq. (5), and critical stress in the Al nanofibers (σ_{Al}) using Eq. (6).

H (GPa)		σ_{flow} (GPa)		σ_{pro} (GPa) Eq. (4)	h_{inc} (nm) Eq. (5)	σ_{Al} (GPa) Eq. (6)
Multilayer	Fibrous	Multilayer	Fibrous			
4.1 ± 0.39	4.9 ± 0.6	2.6 ± 0.25	2.91 ± 0.4	3.84	12	3.1

mapping images are shown separately for Al and Si layers in Figs. 3(d) and 3(e), respectively. The Si layers in close contact with the indent tip have shown layer rotation [marked in the dotted circle in Fig. 3(d)]. Moreover, Fig. 3(d) shows that the amorphous layer of Si is locally fractured near the indenter tip. The true plastic strain, representing layer thickness reduction of the Al layers under the tip along the loading direction, has been obtained by measuring the layer thicknesses at the specified layer locations [marked in Fig. 3(b)], which is

plotted in Fig. 3(e). (The procedure for measuring true plastic strain in the individual Al layers is described in Sec. S4 in the Supplemental Material [26].) The true plastic strains for the Al layer increase from 0% at the sixth layer to 64% at the first layer near the tip. However, the evidence of plastic deformation in the amorphous Si layer was negligible due to lack of measurable reduction in layer thickness of Si.

To provide more insight into the deformed morphology at the C/A interface, a high-angle annular dark field (HAADF)

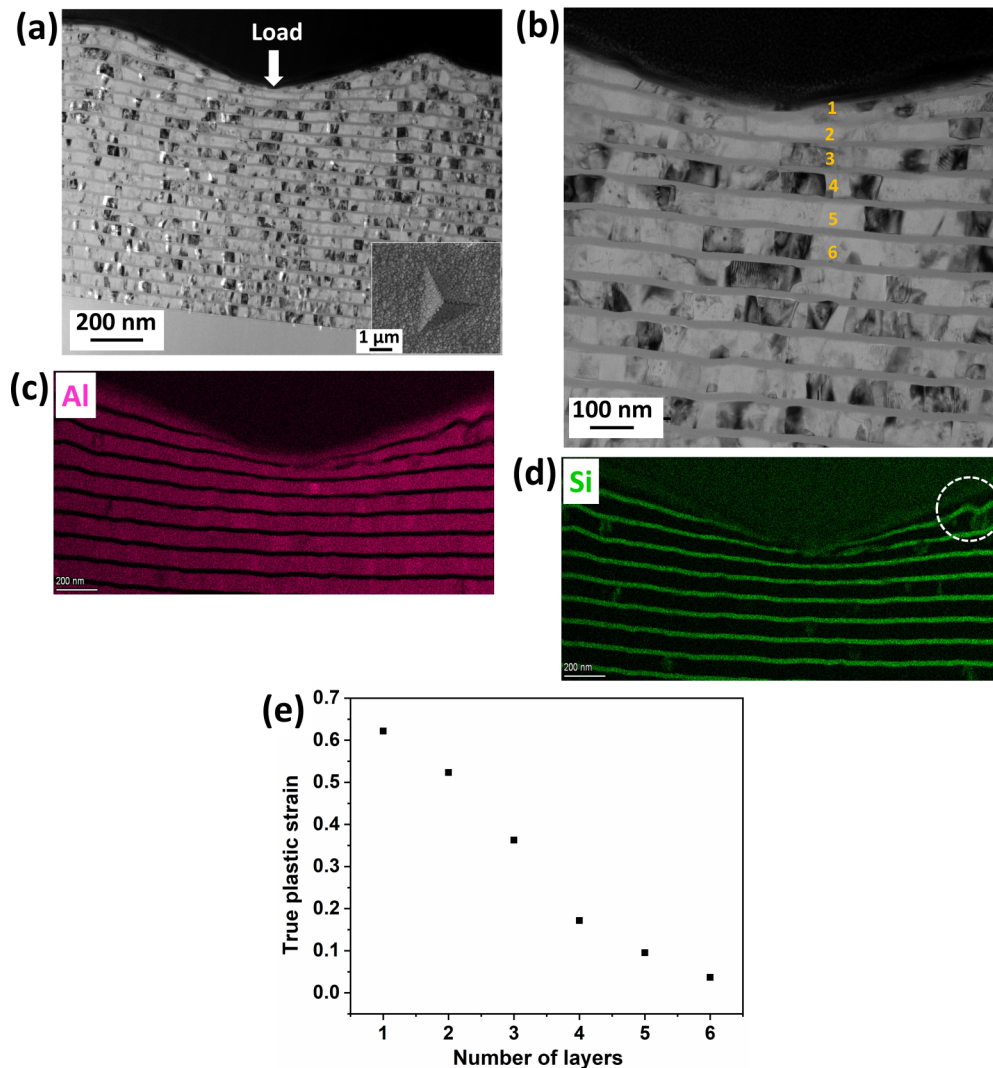


FIG. 3. (a) Transmission electron microscopy (TEM) bright-field image of the cross-section directly under the indent in Al₈₀/Si₂₀ multilayer film having the inset showing the typical indentation impression. (b) High-magnification image of the indentation mark focusing a few layers of Al and Si. (c) and (d) represent the scanning TEM (STEM) elemental mapping of Al and Si layers, respectively. (e) Plot showing the variation of true plastic strain as a function of layer number from (b).

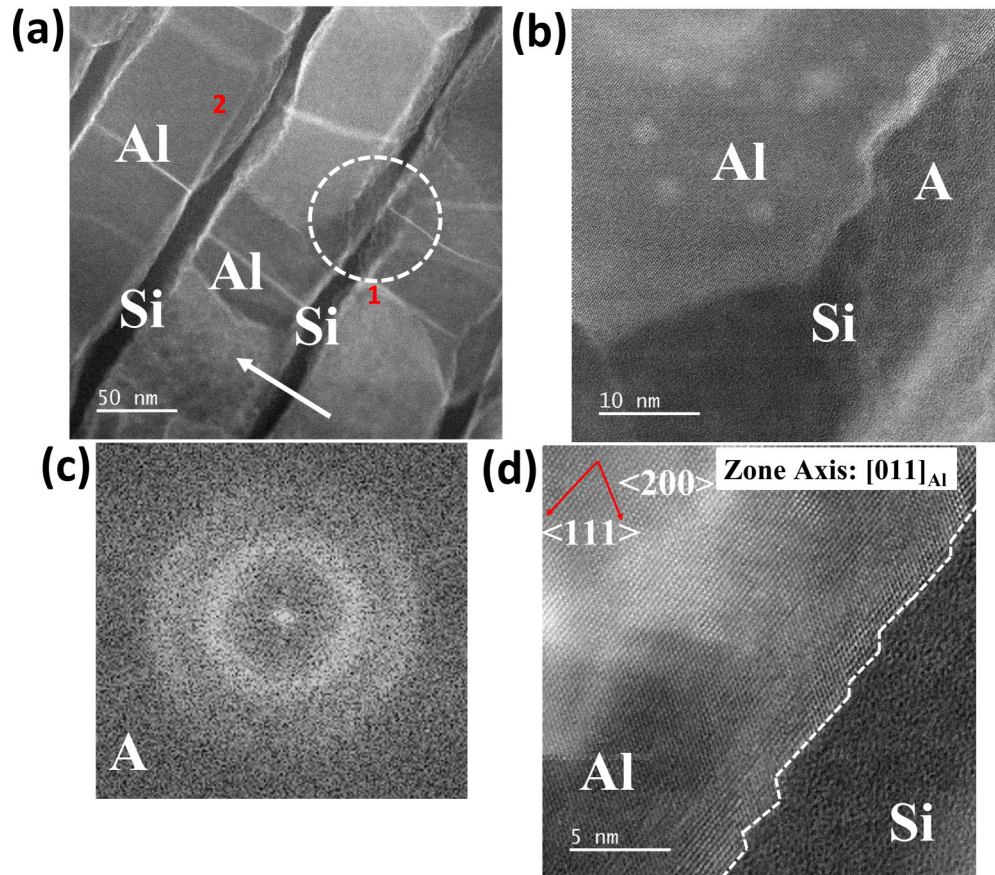


FIG. 4. (a) High-angle annular dark field (HAADF) scanning transmission electron microscopy (STEM) image showing the fracture of the amorphous Si layers within the crystalline Al layers underneath the nanoindents. (b) High-resolution image from the dotted circle of (a). (c) Fast Fourier transform (FFT) of the region marked as A in (b). (d) High-resolution HAADF-STEM image showing the interface of the Al and fractured Si layers below the indent.

STEM image focusing on the fractured Si layers is shown in Fig. 4(a). The arrow denotes the loading direction. Layer 1, which is close to the indentation surface is completely fractured, whereas layer 2 is found to be severely deformed. The high-resolution HAADF micrograph highlighted by the broken circle in Fig. 4(a) is shown in Fig. 4(b). The SBs have been formed near the fracture surface of the Si layer, which appears bright, and the undeformed region is dark, which is a result of thickness contrast [32]. The SBs are formed due to stress concentration in the localized region of the Si layer, which ultimately leads to fracture of the amorphous Si layer. The corresponding FFT pattern of the deformed region A containing the SBs is shown in Fig. 4(c). One of the interesting observations obtained from the fractured Si layer is the formation of the slip steps at the interface of the crystalline Al and amorphous Si layer containing the SBs [Fig. 4(d)] that are likely stress concentration sites that ultimately lead to fracture of the Si layer [10].

The nanoindentation study of the cosputtered Al-Si film reveals a hardness value of 4.9 ± 0.6 GPa, which is higher than that of the Al-Si multilayer (Table I). However, the observed hardness is almost five times lower than that of superhard materials, such as molybdenum bimetallic compounds, due to the presence of carbides and nitrides [33]. The low-magnification BF image of the indented film is shown in Fig. 5(a). The

highlighted region near the indent impression indicates the deformation zone, which can be easily distinguished from the undeformed surrounding zone. An enlarged BF image close to the indent impression shows the formation of deformation inside several Al grains [Fig. 5(b)]. The HRSTEM image from one of the deformed Al grains near the indent reveals the formation of twin boundary, as shown in Fig. 5(c). The measured interplanar spacing verifies that the twin structure corresponds to the (111) plane of Al. The corresponding FFT in Fig. 5(d) confirms the presence of twin-related additional diffraction spots, indicating twinning in the Al grain across the (111) plane.

D. Micropillar compression

Along with the indentation experiment, the strength of the Al-Si multilayer and the Al-Si nanofibrous composite was also determined via the micropillar compression test. Figure 6(a) compares the engineering stress–engineering strain curves, showing the plastic region obtained from micropillar compression testing of the films with nanolaminate and fibrous structure. Figure S3 in Sec. S2 in the Supplemental Material [26] shows the total engineering stress-strain plot including the elastic and plastic part of the films. The results show that the nanolaminate has higher yielding stress and very

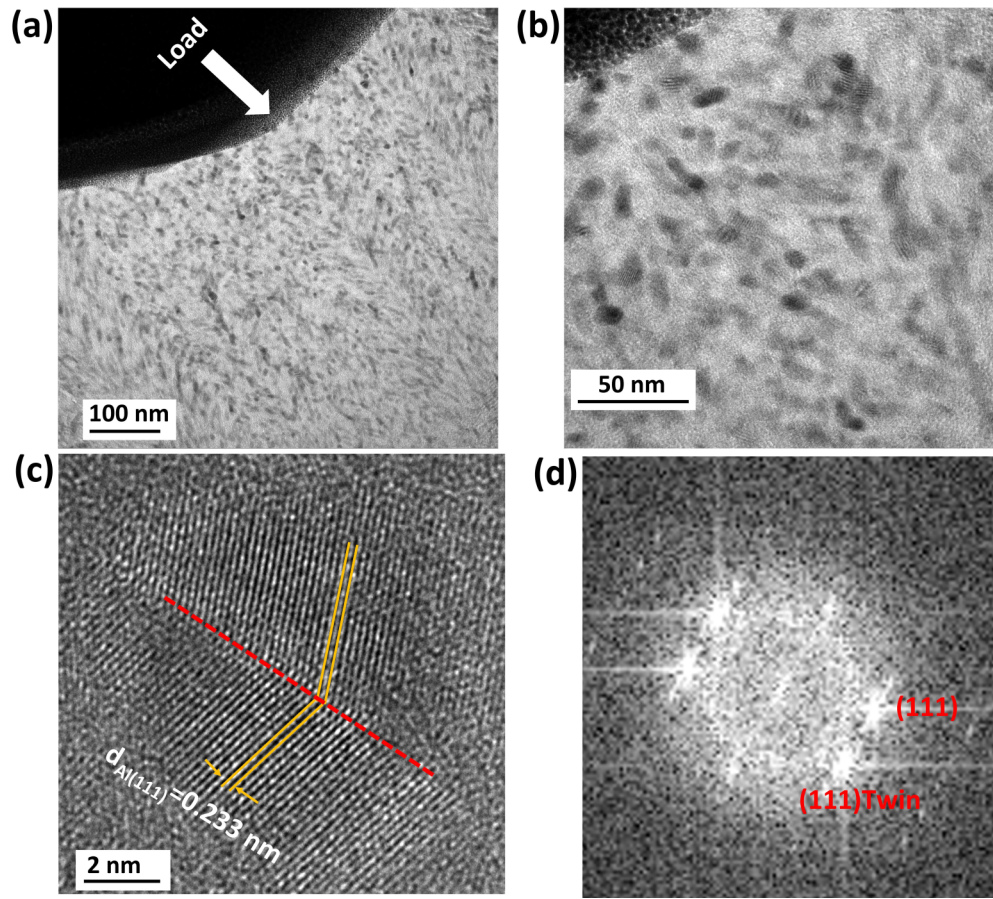


FIG. 5. Representative deformation morphology of indented cosputtered film. (a) Low-magnification bright-field transmission electron microscopy (TEM) image of a cross-section directly under the indent. (b) Enlarged image of the indent showing deformation in the Al nanograins. (c) High-resolution STEM (HRSTEM) BF image showing the twin boundary in the (111) planes of Al. (d) Fast Fourier transform (FFT) pattern from the (111) plane of Al showing the twin structure.

high strain hardening rate; on the other hand, nanofibrous film has lower yielding stress but stable strain hardening. It is found that the Al-Si multilayer exhibits a maximum compressive flow stress value of 2.6 ± 0.25 GPa (Table I). In contrast, the Al-Si fibrous film reveals a higher flow strength value of 2.9 ± 0.4 GPa than the multilayer film. In addition, the multilayer film displays plastic deformation to a plastic

strain of $\sim 14\%$, beyond which the pillar fractures due to shear instability. In contrast, the fibrous film displays uniformly distributed plastic flow, without SB formation, to a plastic strain of $\sim 24\%$, offering better compressive plasticity than the nanolaminate. The plots of both types of films show a similar trend of increasing true stress with true plastic strain, indicating strong strain hardening behavior during plastic de-

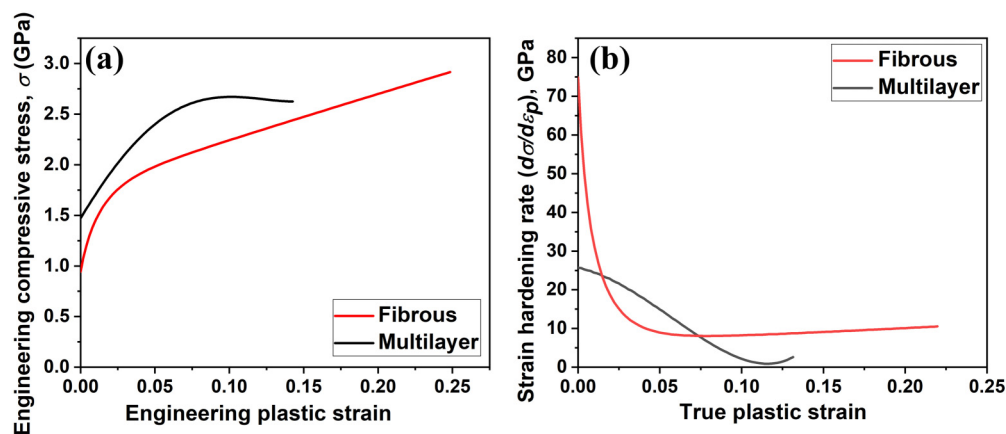


FIG. 6. (a) Engineering stress–engineering plastic strain curves of the multilayer and fibrous film. (b) Plots depicting the variation of strain hardening rate with true plastic strain.

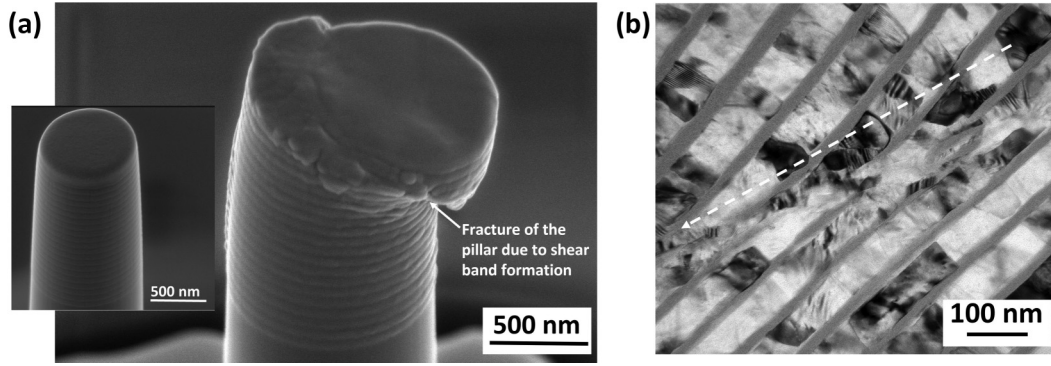


FIG. 7. (a) Scanning electron microscopy (SEM) micrograph of the compressed pillar of the Al₈₀/Si₂₀ multilayer film prepared by focused ion beam (FIB) method. Inset shows the representative SEM image of the pillar before deformation. (b) Transmission electron microscopy (TEM) bright-field image showing the shear bands along the diagonal of the pillar.

formation. Figure 6(b) demonstrates the plots of the strain hardening rate against the true plastic strain for both types of films, which signifies that the fibrous film exhibits a substantial amount of strain hardening as compared with the multilayer film. Figure 7(a) shows a postcompression SEM image of the pillar for multilayer film including the image of the prior-compressed pillar as inset. The deformation morphology shown in Fig. 7(a) corresponds to the onset of the fracture in the multilayer film. After attaining the strain up to $\sim 14\%$, the catastrophic failure of the pillar takes place by forming the barreled shape structure. It is evident from Fig. 7(a) that deformation begins at the upper part of the pillar from one of the corners, presumably due to the higher stress concentration at the top, which separates one half of the barrel from the other. A clear BF TEM image shown in Fig. 7(b) confirms that deformation occurs via SB formation propagating along the diagonal axis of the pillar. The Al layers within the SBs have undergone a severe reduction in thickness as well as grain and/or layer rotation. Furthermore, the brittle Si layers seem to be fractured within the Al layers in Fig. 7(b).

The SEM images of the compressed micropillar of the fibrous film before and after the compression test are depicted in Fig. 8(a). The compressed pillar seems to follow a barrel-shaped morphology with a minute crack emanating from the top surface of the pillar. Further, a couple of TEM micrographs of the compressed micropillar prepared from the fibrous film are shown in Figs. 8(b)–8(e) in a range of magnifications. The barreling effect has been observed in the top half of the pillar without any major crack propagation, which confirms the homogeneous deformation up to a plastic strain value of $\sim 24\%$ [Fig. 8(b)]. Figure 8(c) depicts the zoomed-in micrograph of the pillar focusing on the barreled-shaped location. The fiber-shaped Al grains close to the top corner of the pillar seem to be elongated as specified by the highlighted region in Fig. 8(c). This indicates that the nanofibers of Al undergo plastic deformation compatibly with the surrounding amorphous Si matrix, consistent with the homogeneous deformation of the pillar. The HRSTEM BF micrograph of one of the plastically deformed Al nanofibers is shown in Fig. 8(d). The dimensions of the nanofiber after the plastic deformation have been changed to ~ 100 nm in length and ~ 8 nm in width. TEM examination of the deformed nanofiber revealed a high density of stacking faults (SFs) in

the (111) plane of Al. The presence of SFs was also confirmed according to the extra (111) diffraction spots marked in the FFT image of location A. The presence of such planar defects can be easily differentiated from location B without SFs along with the diffraction pattern.

IV. DISCUSSION

A. Deformation mechanism in Al/Si nanolaminate

1. Stress-strain response: Confined layer slip + strain hardening in Al layer

The presence of heterophase interfaces in multilayer films makes the deformation mechanism distinct from that of the single-layered film. The higher value of strength in the case of multilayer films, as compared with polycrystalline single-layered films, is attributed to the heterophase interfaces, which restrict the dislocation activities. It is well known that multilayer films containing a combination of soft/ductile and hard/brittle phases sustain the plastic flow, which is mostly controlled by the soft/ductile phase [6]. Therefore, considering the confined layer slip (CLS) model, the grain size effect, and geometrically necessary dislocations (GNDs), the flow stress for dislocation glide in the Al matrix can be expressed as [6,34,35]

$$\sigma_{\text{flow}} = M \frac{G}{8\pi t} b \left(\frac{4 - \nu}{1 - \nu} \right) \ln \frac{\alpha t'}{b} + \alpha' G b \sqrt{\frac{\varepsilon_p 2\sqrt{3}}{bt}} + \frac{k}{d^{1/2}}, \quad (3)$$

where $M \sim 3.1$ is the Taylor factor, $b \sim 0.286$ nm is the Burgers vector magnitude in Al, $\nu \sim 0.34$ is Poisson's ratio of Al, k is the Hall-Petch slope (0.07 MPa $\text{m}^{0.5}$) [23], d is the grain size (~ 40 nm), G is the shear modulus of the Al (~ 26.1 GPa), the core cutoff factor $\alpha = 0.6$, interfiber spacing $t = 20$ nm, and projected length of slip plane $t' = t / \cos 45^\circ$ nm, where 45° is the angle between 111_{Al} and interface normal, and $\alpha' = 0.2$. The calculated curve is shown in Fig. 9 for the crystalline Al layer. Equation (3) is an estimation of the flow stress for the polycrystalline Al layer based on the CLS unit mechanism and using the Taylor factor to convert to normal stress for the polycrystal and include additional hardening contributions from grain boundaries in the Al layer and strain hardening due to GND arrays that form due to incompatibility between plastically deforming Al and elastically deforming

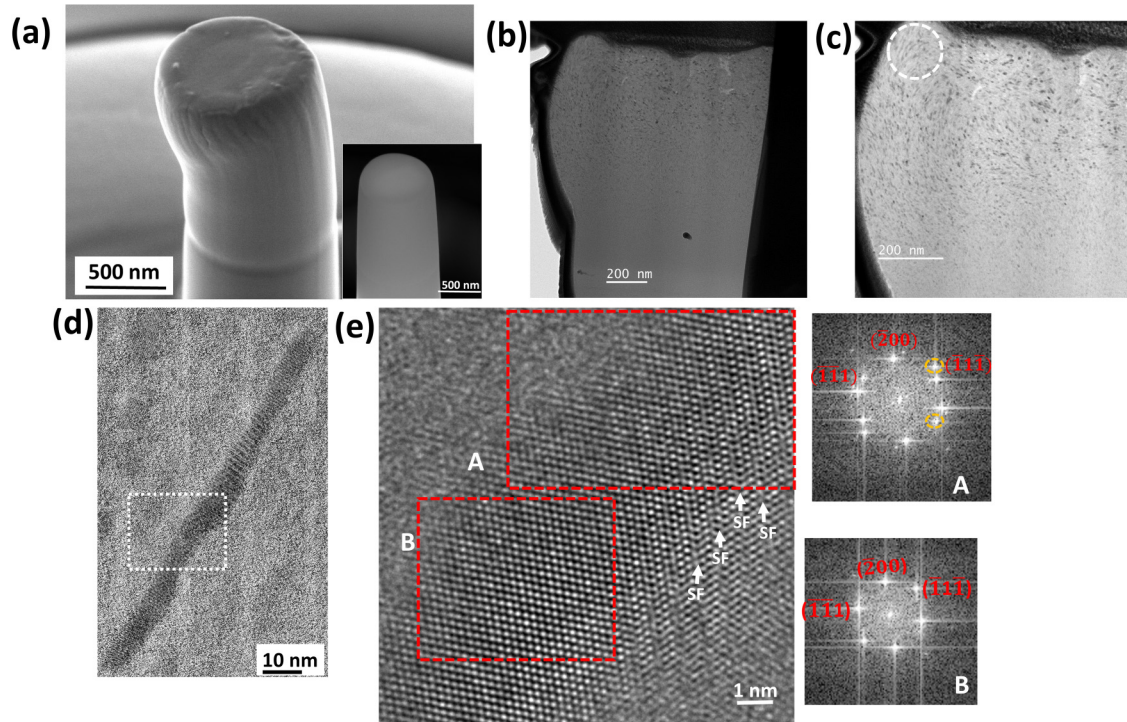


FIG. 8. (a) Scanning electron microscopy (SEM) micrograph of the compressed pillar prepared from the fibrous film having the inset showing the pillar before compression. Transmission electron microscopy (TEM) micrographs of the compressed pillar. (b) Low-magnification bright-field (BF) image. (c) Enlarged BF image. (d) High-resolution STEM (HRSTEM) BF image showing one plastically deformed nanofiber of Al. (e) HRSTEM image from the highlighted dotted square in (d). Inset images of (e) shows the fast Fourier transform (FFT) patterns from the dotted red rectangular markers of the locations A and B.

Si. The strain hardening contribution is assumed to linearly scale inversely with dislocation array spacing or directly with applied strain. With these assumptions, the calculation from Eq. (3) can be superimposed on the experimental stress-strain plot for comparison. The model predicts flow strengths comparable with experimentally measured flow strengths at low plastic strains where strain hardening is highest in Al due to GNDs as the rigid amorphous Si phase deforms elasti-

cally [36]. Equation (3) overpredicts the flow strength with increasing plastic strain where the SB-mediated deformation prevails in the amorphous Si phase, thereby reducing the strain hardening, which will be discussed in the next section. When the intrinsic size decreases to this scale (<100 nm), the chances of dislocation activities in the smaller volume decrease dramatically, and eventually, the dislocation is produced predominantly from the interfaces. Knorr *et al.* [27] reported on the deformation of nanocrystalline Cu/metallic glass Pd-Si multilayer films in which the deformation initiated in the softer Cu layer, leading to accumulation of GNDs at the C/A interfaces and enhancement of the overall strength of the multilayer film.

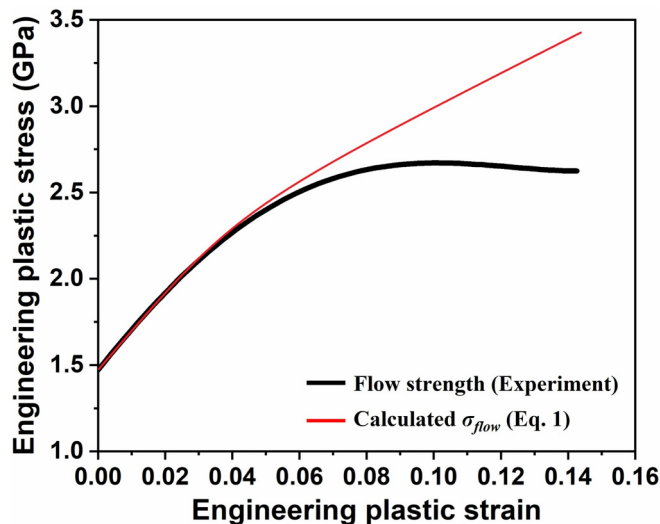


FIG. 9. Calculated σ_{flow} from Eq. (3) for the crystalline Al layer.

2. SB formation in C/A/C nanolaminate

Morphology of the indented film [Fig. 2(b)] as well as the compressed pillar [Fig. 5(c)] suggests that the soft Al phase has preferentially thinned down in between the brittle Si phases due to strength disparity between the two constituent phases. This observation is in good agreement with some previous studies in crystal/metallic glass Cu/Cu50Zr50 pillars [11], C/C Al/Pd [37], and Cu/Zr multilayer films [4]. Systematic slip activity of a single dislocation takes place in the soft Al layer, whereas the low shear strength of the C/A interface is responsible for sliding [6]. However, Wang *et al.* [3] mentioned that, as the deformation starts, activation of a few shear transformation zones (STZs) in an uncorrelated fashion could be possible in the amorphous layer. Nucleation

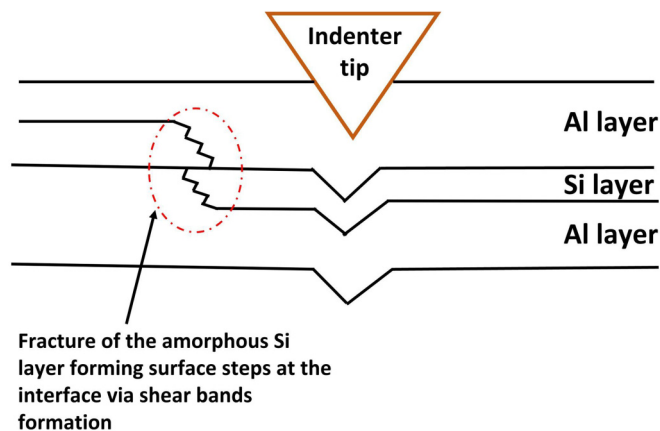


FIG. 10. Schematic representation of the deformation mechanism in the multilayer below the indenter tip.

of the dislocations in the crystalline phase and the subsequent propagation to the next C/A interface activates more STZs in a correlated fashion. Further, as the deformation continues, the activated STZs trigger more adjacent STZs, and the entire inelastic deformation zone diffuses into the deeper amorphous layer. Thus, the cooperative movement of a cluster of STZs leads to the formation of SBs [38]. However, propagation of SBs is only possible if the applied stress reaches the critical value. This is the reason why the amorphous Si layer is shear fractured due to propagation of the SBs at a higher value of applied stress, which is schematically illustrated in Fig. 10. The formation of SBs at the localized region of the thin Si layer due to stress concentration by the applied load leads to shear instability. This commences the catastrophic failure of the brittle Si layer by forming surface steps at the interface of the amorphous Si and crystalline Al layer.

In this paper, micropillar compression of the crystalline Al/amorphous Si multilayer film could avoid the formation of SBs up to 14% of the strain because the thin glassy Si layers are geometrically confined by crystalline layers that elastically counteract the formation of shear steps at the interfaces. This requires that the crystalline layer is sufficiently stiff to produce a substantial elastic force opposing the nucleation of a shear step [7]. After a further increase in strain, barreling of the C/A micropillar is evident [Fig. 7(a)], which is accompanied by localized shear deformation. The localized shear deformation starts by simultaneous rotation of the layer structure as well as fracture of the amorphous Si layer by promoting SBs in the C/A multilayers because the applied stress is considerably greater than the stress required for activation of SBs. Such interlayer SB formation via nanoindentation and micropillar compression have also been observed in a variety of multilayer films [39–41].

The transition of the codeformation mode between the soft crystalline and amorphous layers to fracture of the multilayer is governed by the initiation of SBs, which is controlled by the shear stress. To represent the SB formation quantitatively, a previously demonstrated energy balance model has been applied in this paper. According to the model, the SB is considered as a crack driven by the release of all of the stored elastic energy in the sample [6,42,43]. The mathematical re-

lation, which is analogous to Griffith's crack equation, can be used to estimate the critical stress required to drive a SB as follows:

$$\sigma_{\text{pro}} = \sqrt{\frac{2\sqrt{2}\Gamma E}{h}}, \quad (4)$$

where $\Gamma \sim 0.56 \text{ J m}^{-2}$ [43] is the SB energy per unit area, $E \sim 187 \text{ GPa}$ is Young's modulus of Si, and h is the thickness of the amorphous Si layer. According to the above relation, the stress required to drive a SB propagation (σ_{pro}) increases with the decrease in amorphous layer thickness, which is estimated to be 3.84 GPa for a thickness of 20 nm of the amorphous Si layer (Table I). Authors of earlier reports suggest that there exists a critical characteristic dimension of layer thickness $h_{\text{cri}} \sim 60 \text{ nm}$ below which the deformation mechanism of the amorphous phase shifts from localized shear failure to homogeneous deformation [6,42,43]. For a thinner amorphous layer thickness ($> h_{\text{cri}}$), the nucleated embryonic SB remains stable at the stress required for homogeneous deformation.

As proposed by an aged-rejuvenation-glass-liquid SB model, no STZ will grow into a mature SB, if the thickness of the amorphous layer is below some critical value. According to this model, the localized glassy region should exceed an incubation length scale h_{inc} to develop STZ to a mature SB [3,6]:

$$h_{\text{inc}} = \frac{\mathcal{E} C_v^2 (T_g - T_{\text{env}})^2}{c_s \tau_{\text{glue}}^2}, \quad (5)$$

where \mathcal{E} is the thermal diffusivity of amorphous Si ($0.062 \times 10^{-4} \text{ m}^2/\text{s}$) [44], C_v is its volumetric specific heat of Si [45,46], T_{env} (300 K) is the ambient temperature, $\tau_{\text{glue}} \approx 0.1E$, T_g is the glass transition temperature of amorphous Si (1000 K) [44], $C_s = (\mu/\rho)^{0.5}$ is the shear wave speed [47,48]. Considering the amorphous Si in this paper, Eq. (3) gives $h_{\text{inc}} = 12 \text{ nm}$, which is well satisfied with earlier studies ranging from 5 to 10 nm [47,48]. Therefore, it can be expected that, for a layer thickness lower than h_{inc} , it is almost impossible to nucleate SBs. In a regime of $h_{\text{inc}} < h_a < h_{\text{cri}}$, although the SBs can be formed, the thin amorphous layer will be firmly constrained by the ductile Al layers, which is responsible for the macroscopic homogeneous-like deformation in the crystalline Al/covalent amorphous Si multilayer film. Through investigation of the tensile behavior of crystalline Cu/metallic glass CuZr nanolaminates, Kim *et al.* [49] reported that SB instability can be avoided by the presence of a 5- to 10-nm-thick glassy layer, which also acts as high-capacity sinks for dislocations, enabling absorption of free volume and free energy transported by the dislocations.

B. Deformation mechanism in the fibrous film

1. Partial dislocation-mediated uniform plasticity in Al nanofibers

The higher compressive plasticity of the film with nanofibers of Al embedded in amorphous Si matrix obtained through the compression of the micropillar is attributed to the homogeneous deformation up to plastic strain exceeding 20%. The homogeneous plastic flow without any fracture is also suggestive of the absence of any detectable SBs in the deformed morphologies. The nanofibers of Al have under-

gone plastic deformation, which actively participates in the homogeneous deformation of the film. The elongation of the Al fibers due to the compression test, as evident from the TEM micrograph [Fig. 8(c)] close to the top surface, suggests that the homogeneous deformation prevails over the localized shear deformation. The enlarged HRSTEM shown in Fig. 8(d) witnessed the formation of the high density of SFs inside the (111) planes of the elongated Al fibers. Along with this, the twin boundary in (111) planes of Al grains [Fig. 5(c)] has been observed close to the indent impression. The existence of SFs and twin structure inside the Al grains is beneficial in preventing the slip of dislocations and the propagation of cracks, thereby improving the compressive plasticity of the fibrous film. Earlier, it has been postulated that, in nanoscale grains, emission of partials from grain boundaries or interfaces is considered a driving mechanism for deformation in various nanocrystalline systems [18]. Authors of earlier studies have reported that, although Al has high SF energy (SFE), formation of a high density of wide SFs is possible in nanocrystalline Al due to emission of partial dislocations from grain boundaries [50,51]. Therefore, it is expected that, for such nanofibers of Al, the effective underlying deformation mechanism is the generation and absorption of partial dislocations at grain boundaries and/or interfaces, which serve as the sinks and sources for dislocations. The critical stress required to initiate partial dislocations in the crystalline Al (σ_{Al}) can be calculated by considering the SFE (γ_{SFE}), which is given as follows [18,52]:

$$\sigma_{Al} = \frac{2\phi\mu_{Al}b_{Al}}{d} + \frac{\gamma_{SFE}}{b_{Al}}. \quad (6)$$

Here, μ_{Al} is the shear modulus of Al (~ 35 GPa), α reflects the character of dislocation (~ 0.5 for edge dislocation), and d is the grain size of the Al nanofibers, which is ~ 40 nm, as estimated from the TEM. The predicted value of σ_{Al} from Eq. (6) fits well with the experimental results of strength value of cosputtered film obtained through micropillar compression, see Table I. In addition, due to the Al-Si cosputtering, it is inevitable that some Si solute atoms will be trapped in the Al nanofibers. Gong *et al.* [53] performed first-principles density function theory calculations and found that Si can significantly reduce the SFE of Al on {111} planes from 150 to 100 mJ/m² at Si solute concentration of 12.5 at.%. It is postulated that the lowering of SFE of Al facilitates the partial dislocation-mediated glide resulting in the formation of wide SFs extending across the width of Al nanofibers. One of the possible reasons for the higher flow strength observed experimentally in the case of the fibrous film is attributed to the homogeneous distribution of the finer Al fibers having grain size of 40 nm as compared with the individual length scale of the cosputtered film, i.e., 80 nm.

2. Plasticity mechanism in nano-amorphous Si channels

TEM characterization (Fig. 8) did not reveal any SBs in the amorphous Si phase of the fibrous film. The mechanism of plastic deformation of the film with fibrous morphology through inhibition of the SBs formation is illustrated by the schematic view shown in Fig. 11. The plastic zone below the indent tip suggests that the nanofibers of Al have deformed

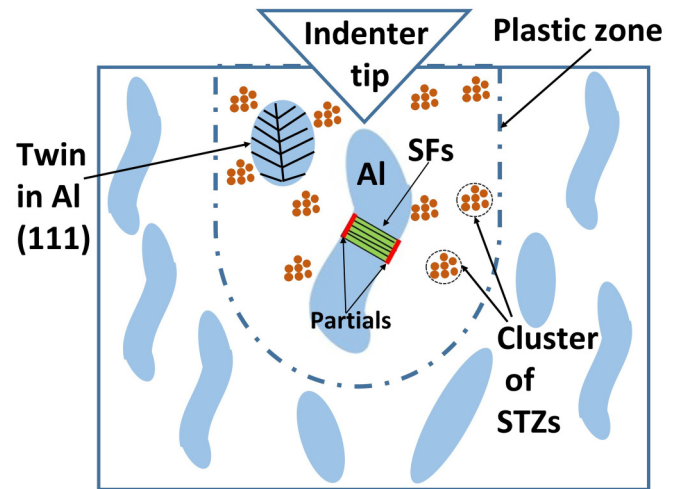


FIG. 11. Schematic representation of the deformation mechanism in film with fibrous morphology.

plastically by formation of a wide SF through the leading partial traversing total width of the Al fiber as well as deformation twins, which clearly explain our experimental observation. Although the volume fraction of Al is higher than that of Si, there is a continuous amorphous Si network of size ~ 20 nm forming a nanochannel in between the Al nanofibers. The cluster of STZs formed in the nanochannels of Si network inside the plastic zone are distributed randomly around the deformed nanofibers of Al. We postulate that, along with nanofibers of Al, the STZs formed in the amorphous Si phase also experience the homogeneous plastic flow. It is suspected that, the STZs cannot reach the critical size, as the applied stress is lower than the critical value of stress required for the formation of mature SBs due to the presence of nanofibers of Al. This implies a higher value of strength with a higher plastic strain and strain hardening rate in the nanofibrous morphology of Al embedded in the amorphous Si matrix, which suppresses the localized fracture through SB formation. Using MD simulation, Fan *et al.* [54] reported that the formation of ductile dimples in amorphous CuNb layers in Cu-CuNb nanolaminate could be related to the generations of abundant STZs, which restricts the propagation of SBs. Further, it must be noted here that higher strength in the case of the fibrous film is not only due to homogeneous deformation in the Al and Si phase but also to the higher phase fraction of the hard Si phase (i.e., 37 vol.%) than that of multilayer film (i.e., Si layer thickness ≈ 20 nm).

Wang *et al.* [55] studied the tensile-compressive behavior in amorphous Si film by an experimental technique, which revealed the homogeneous plastic flow after yielding at lower value of stress ($\sigma_y \sim 4.5$ GPa) during compressive behavior, whereas tensile loading gives a sudden failure without yielding at higher stress ($\sigma_y \sim 6.5$ GPa). Therefore, they concluded that amorphous Si is much stronger in tension, whereas it is more ductile under compression. To investigate the reason behind this, authors of earlier studies elucidate that plastic deformation in amorphous Si is related to the atomic structure of the material. In comparison with amorphous

Si, the other metallic glasses exhibit apparent differences in terms of compositions, atomic packing, and in bonding. They are generally multicomponent, having nearly spherically symmetric nondirectional metallic bonding between atoms with considerable differences in atomic radii of the different chemical components. In contrast, amorphous silicon is a space network solid with quasi-isotropically directed primary covalent bonds. Compression lowers the activation barrier of shear transformations to facilitate yielding. The increase in coordination number >4 is associated with deformation-induced fertile sites for shear transformation, thus suggesting local transformation from tetrahedral atomic environments to higher-coordinated structures with a greater fraction of yielding in the plastic deformation regime. Authors of earlier studies on the indentation behavior of amorphous Si film using advanced techniques, such as *in situ* Raman spectroscopy, reported that the tetrahedral network of amorphous Si undergoes a local change in bond angles and bond length without modification to the original atomic coordination of the network at a lower value of strain giving rise to elastic deformation [56]. At a greater value of the applied load, the increased distortions (disorder) of the tetrahedral network lead to the formation of more closely packed atomic arrangements, i.e., in the form of predominately fivefold coordinated defects in the strained amorphous Si. The occurrence of fivefold coordinated defects during indentation appears to be a sign of plastic deformation of the amorphous Si thin film. These fivefold coordinated atoms or so-called *liquidlike particles* act as the carriers for plasticity in amorphous Si, analogous to dislocations in crystalline materials. In addition, it is noted that Al atoms will mix in amorphous Si matrix due to the Al-Si cosputtering. Compared with the strong Si-Si bonds, Al-Si bonds have lower strength which will decrease the flow strength of amorphous Si and promote plastic flow. Our MD simulations demonstrated well the decrease in flow strength of amorphous Si with the increase in the concentration of the Al element (see Fig. S1(b) in Sec. S1 in the Supplemental Material [26]).

V. CONCLUSIONS

In this paper, we have revealed the significance of the microstructure morphology, in addition to the size, in controlling the deformation behavior of crystalline Al/covalently bonded

amorphous Si thin films. The key conclusions are summarized as follows:

(1) Nanofibrous morphology consisting of amorphous Si matrix and crystalline Al fibers of finer size distribution, i.e., $\sim 15\text{--}20$ nm in diameter, $40\text{--}50$ nm in length, and 20 nm interfiber spacing, exhibits high nanoindentation hardness (4.9 GPa), maximum compressive flow strength (2.91 GPa), and strain hardening behavior without any detectable SBs to plastic strains of $\sim 24\%$. In addition, superior strength of the fibrous film is ascribed to the higher phase fraction of the hard Si phase than the individual length scale of the amorphous Si layer in the case of the multilayer film. Plasticity in nanofibers of Al appears to be mediated by creating a twin boundary as well as partial dislocations producing a high density of closely spaced SFs on $\{111\}$ planes, resulting in uniform extension of the nanofibers. In the absence of detectable SBs, it is postulated that plasticity in amorphous Si involved a high density of STZs that do not grow to a critical size due to nanoscale dimension of amorphous Si that inhibits the transition from STZ to localized SB. Furthermore, the applied shear stress is presumably lower than the critical stress required for the activation of a mature SB.

(2) In contrast, the nanolaminate morphology, 80 nm crystalline Al/ 20 nm amorphous Si, exhibited SBs and no evidence of layer thickness reduction in Si underneath the nanoindenters as well as under micropillar compression. Plasticity was confined in the crystalline Al layers with the flow stress as a function of plastic strain interpreted using unit mechanisms of single dislocations confined between Si/Al/Si interfaces, columnar grain boundaries in Al and strain hardening from dislocation arrays resulting from CLS. The nanolaminate experiences homogeneous plastic deformation, up to $\sim 5\text{--}10\%$ plastic strain, until the applied stress reaches the critical value to drive the SBs.

ACKNOWLEDGMENTS

B.P.S., W.W., J.W., and A.M. acknowledge funding from the Department of Energy, Office of Science, Office of Basic Energy Sciences (Grant No. DE-SC0016808). B.P.S. would like to thank Michigan Center for Materials Characterization for nanoindentation and microstructural observation of the films.

-
- [1] K. Ming, Z. Zhu, W. Zhu, B. Fang, B. Wei, P. K. Liaw, X. Wei, J. Wang, and S. Zheng, Enhancing strength and ductility via crystalline-amorphous nanoarchitectures in TiZr-Based alloys, *Sci. Adv.* **8**, eabm2884 (2022).
- [2] Y. Cui, O. T. Abad, F. Wang, P. Huang, T. J. Lu, K. W. Xu, and J. Wang, Plastic deformation modes of CuZr/Cu multilayers, *Sci. Rep.* **6**, 23306 (2016).
- [3] Y. Wang, J. Li, A. V. Hamza, and T. W. Barbee, Ductile crystalline-amorphous nanolaminates, *Proc. Natl. Acad. Sci. USA* **104**, 11155 (2007).
- [4] J. Y. Zhang, Y. Liu, J. Chen, Y. Chen, G. Liu, X. Zhang, and J. Sun, Mechanical properties of crystalline Cu/Zr and crystalline Cu/Cu-Zr multilayers, *Mater. Sci. Eng. A* **552**, 392 (2012).
- [5] W. Guo, E. Jäggle, J. Yao, V. Maier, S. Korte-Kerzel, J. M. Schneider, and D. Raabe, Intrinsic and extrinsic size effects in the deformation of amorphous CuZr/nanocrystalline Cu nanolaminates, *Acta Mater.* **80**, 94 (2014).
- [6] J. Y. Zhang, G. Liu, S. Y. Lei, J. J. Niu, and J. Sun, Transition from homogeneous-like to shear-band deformation in nanolayered crystalline Cu/amorphous Cu-Zr micropillars: intrinsic vs. extrinsic size effect, *Acta Mater.* **60**, 7183 (2012).
- [7] A. Donohue, F. Spaepen, R. G. Hoagland, and A. Misra, Suppression of the shear band instability during plastic flow of

- nanometer-scale confined metallic glasses, *Appl. Phys. Lett.* **91**, 89 (2007).
- [8] I. Knorr, N. M. Cordero, E. T. Lilleodden, and C. A. Volkert, Mechanical behavior of nanoscale Cu/PdSi multilayers, *Acta Mater.* **61**, 4984 (2013).
- [9] Z. Fan, Y. Liu, S. Xue, R. M. Rahimi, D. F. Bahr, H. Wang, and X. Zhang, Layer thickness dependent strain rate sensitivity of Cu/amorphous CuNb multilayer, *Appl. Phys. Lett.* **110**, 161905 (2017).
- [10] Z. Fan, Q. Li, J. Li, S. Xue, H. Wang, and X. Zhang, Tailoring plasticity of metallic glasses via interfaces in Cu/Amorphous CuNb laminates, *J. Mater. Res.* **32**, 2680 (2017).
- [11] M. C. Liu, C. J. Lee, Y. H. Lai, and J. C. Huang, Microscale deformation behavior of amorphous/nanocrystalline multilayered pillars, *Thin Solid Films* **518**, 7295 (2010).
- [12] H. S. Chou, X. H. Du, C. J. Lee, and J. C. Huang, Enhanced mechanical properties of multilayered micropillars of amorphous ZrCuTi and nanocrystalline Ta layers, *Intermetallics* **19**, 1047 (2011).
- [13] A. Bharathula, S. W. Lee, W. J. Wright, and K. M. Flores, Compression testing of metallic glass at small length scales: effects on deformation mode and stability, *Acta Mater.* **58**, 5789 (2010).
- [14] J. Y. Kim, D. Jang, and J. R. Greer, Nanolaminates utilizing size-dependent homogeneous plasticity of metallic glasses, *Adv. Funct. Mater.* **21**, 4550 (2011).
- [15] D. Tönnies, R. Maaß, and C. A. Volkert, Room temperature homogeneous ductility of micrometer-sized metallic glass, *Adv. Mater.* **26**, 5715 (2014).
- [16] J. D. Schuler, C. M. Grigorian, C. M. Barr, B. L. Boyce, K. Hattar, and T. J. Rupert, Amorphous intergranular films mitigate radiation damage in nanocrystalline Cu-Zr, *Acta Mater.* **186**, 341 (2020).
- [17] A. Borroto, S. Bruyère, N. Thurieau, C. Gendarme, E. Jimenez-Piqué, J. J. Roa, J. F. Pierson, F. Mücklich, and D. Horwat, Structural and mechanical properties of $Zr_{1-x}Mo_x$ thin films: from the nano-crystalline to the amorphous state, *J. Alloys Compd.* **729**, 137 (2017).
- [18] J. T. Zhao, J. Y. Zhang, L. F. Cao, Y. Q. Wang, P. Zhang, K. Wu, G. Liu, and J. Sun, Zr alloying effect on the microstructure evolution and plastic deformation of nanostructured Cu thin films, *Acta Mater.* **132**, 550 (2017).
- [19] B. P. Sahu, A. Dutta, and R. Mitra, Influence of composition on nanoindentation response of Ni-Zr alloy thin films, *Metall. Mater. Trans. A* **50**, 5656 (2019).
- [20] B. P. Sahu, C. K. Sarangi, and R. Mitra, Effect of Zr content on structure property relations of Ni-Zr alloy thin films with mixed nanocrystalline and amorphous structure, *Thin Solid Films* **660**, 31 (2018).
- [21] R. Horie, N. Yasui, Y. Ohashi, and T. Den, Substrate bias effect on Al-Si and Al-Ge thin film structure, *Thin Solid Films* **516**, 8315 (2008).
- [22] K. Fukutani, K. Tanji, T. Saito, and T. Den, Phase-separated Al-Si thin films, *J. Appl. Phys.* **98**, 033507 (2005).
- [23] V. Radmilović, D. Mitlin, and U. Dahmen, Ultra-hard nanostructured Al-Si thin films, *Mater. Sci. Forum* **494**, 13 (2005).
- [24] H. Sitinamaluwa, J. Nerkar, M. Wang, S. Zhang, and C. Yan, Deformation and failure mechanisms of electrochemically lithiated silicon thin films, *RSC Adv.* **7**, 13487 (2017).
- [25] B. Wei, W. Wu, D. Xie, H. H. Lien, M. Kayitmazbatir, A. Misra, and J. Wang, *In situ* characterization of tensile behavior of laser rapid solidified Al-Si heterogeneous microstructures, *Mater. Res. Lett.* **9**, 507 (2021).
- [26] See Supplemental Material at <http://link.aps.org/supplemental/10.1103/PhysRevMaterials.6.094002> for Sec. S1, Elemental STEM mapping of the cosputtered film; Sec. S2, Calculation of true plastic strain in Al layers; Sec. S3, Effect of taper angle on the engineering stress-strain curves; and Sec. S4, Atomistic simulations of Si-Al system. The Supplemental Material also contains Refs. [57–60].
- [27] J. R. Greer, W. C. Oliver, and W. D. Nix, Size dependence of mechanical properties of gold at the micron scale in the absence of strain gradients, *Acta Mater.* **53**, 1821 (2005).
- [28] J. Wang, C. Yang, and P. D. Hodgson, Strain gradients in Cu-Fe thin films and multilayers during micropillar compression, *Mater. Sci. Eng. A* **651**, 146 (2016).
- [29] M. Nasim, Y. Li, M. Dargusch, and C. Wen, Ultra-strong and ductile Ta/Co nanolaminates strengthened via grain-boundary expanding and interfacial sliding, *Appl. Mater. Today* **23**, 100983 (2021).
- [30] I. N. Sneddon, The relation between load and penetration in the axisymmetric Boussinesq problem for a punch of arbitrary profile, *Int. J. Engng. Sci.* **3**, 47 (1965).
- [31] U. Barajas-Valdes and O. M. Suárez, Nanomechanical properties of thin films manufactured via magnetron sputtering from pure aluminum and aluminum-boron targets, *Thin Solid Films* **693**, 137670 (2020).
- [32] W. H. Jiang and M. Atzmon, The effect of compression and tension on shear-band structure and nanocrystallization in amorphous $Al_{90}Fe_5Gd$: A high-resolution transmission electron microscopy study, *Acta Mater.* **51**, 4095 (2003).
- [33] D. Errandonea, J. A. Sans, D. Santamar, O. Gomis, and F. Sapi, Compressibility and structural stability of ultra-incompressible bimetallic interstitial carbides and nitrides, *Phys. Rev. B* **85**, 144103 (2012).
- [34] A. Misra, J. P. Hirth, and R. G. Hoagland, Length-scale-dependent deformation mechanisms in incoherent metallic multilayered composites, *Acta Mater.* **53**, 4817 (2005).
- [35] D. Bhattacharyya, N. A. Mara, P. Dickerson, R. G. Hoagland, and A. Misra, Compressive flow behavior of Al-TiN multilayers at nanometer scale layer thickness, *Acta Mater.* **59**, 3804 (2011).
- [36] J. Wang and A. Misra, Strain hardening in nanolayered thin films, *Curr. Opin. Solid State Mater. Sci.* **18**, 19 (2014).
- [37] P. Dayal, M. Z. Quadir, C. Kong, N. Savvides, and M. Hoffman, Transition from dislocation controlled plasticity to grain boundary mediated shear in nanolayered aluminum/palladium thin films, *Thin Solid Films* **519**, 3213 (2011).
- [38] B. P. Sahu, A. Dutta, and R. Mitra, Mechanism of negative strain rate sensitivity in metallic glass film, *J. Alloys Compd.* **784**, 488 (2019).
- [39] B. P. Sahu, W. H. Higgins, B. K. Derby, G. M. Pharr, and A. Misra, Strain-rate dependent deformation mechanisms in single-layered Cu, Mo, and multilayer Cu/Mo thin films, *Mater. Sci. Eng. A* **838**, 142776 (2022).
- [40] D. Bhattacharyya, N. A. Mara, P. Dickerson, R. G. Hoagland, and A. Misra, A transmission electron microscopy study of the deformation behavior underneath nanoindentations in nanoscale Al-TiN multilayered composites, *Philos. Mag.* **90**, 1711 (2010).
- [41] D. Bhattacharyya, N. A. Mara, P. Dickerson, R. G. Hoagland, and A. Misra, Transmission electron microscopy study of the

- deformation behavior of Cu/Nb and Cu/Ni nanoscale multilayers during nanoindentation, *J. Mater. Res.* **24**, 1291 (2009).
- [42] D. Jang and J. R. Greer, Transition from a strong-yet-brittle to a stronger-and-ductile state by size reduction of metallic glasses, *Nat. Mater.* **9**, 215 (2010).
- [43] C. Q. Chen, Y. T. Pei, and J. T. M. De Hosson, Effects of size on the mechanical response of metallic glasses investigated through in situ TEM bending and compression experiments, *Acta Mater.* **58**, 189 (2010).
- [44] T. Kemp, T. A. S. Srinivas, R. Fetting, and W. Ruppel, Measurement of thermal diffusivity of thin films and foils using a laser scanning microscope, *Rev. Sci. Instrum.* **66**, 176 (1995).
- [45] M. Zeneli, I. Malgarinos, A. Nikolopoulos, N. Nikolopoulos, P. Grammelis, S. Karellas, and E. Kakaras, Numerical simulation of a silicon-based latent heat thermal energy storage system operating at ultra-high temperatures, *Appl. Energy* **242**, 837 (2019).
- [46] A. K. Ray, D. Rakshit, K. Ravi Kumar, and H. Gurgenci, Silicon as high-temperature phase change medium for latent heat storage: a thermo-hydraulic study, *Sustain. Energy Technol. Assessments* **46**, 101249 (2021).
- [47] F. Shimizu, S. Ogata, and J. Li, Yield point of metallic glass, *Acta Mater.* **54**, 4293 (2006).
- [48] F. Shimizu, S. Ogata, and J. Li, Theory of shear banding in metallic glasses and molecular dynamics calculations, *Mater. Trans.* **48**, 2923 (2007).
- [49] J. Y. Kim, X. Gu, M. Wraith, J. T. Uhl, K. A. Dahmen, and J. R. Greer, Suppression of catastrophic failure in metallic glass-polyisoprene nanolaminate containing nanopillars, *Adv. Funct. Mater.* **22**, 1972 (2012).
- [50] X. Z. Liao, S. G. Srinivasan, Y. H. Zhao, M. I. Baskes, Y. T. Zhu, F. Zhou, E. J. Lavernia, and H. F. Xu, Formation mechanism of wide stacking faults in nanocrystalline Al, *Appl. Phys. Lett.* **84**, 3564 (2004).
- [51] X. Z. Liao, F. Zhou, E. J. Lavernia, S. G. Srinivasan, M. I. Baskes, D. W. He, and Y. T. Zhu, Deformation mechanism in nanocrystalline Al: partial dislocation slip, *Appl. Phys. Lett.* **83**, 632 (2003).
- [52] M. Chen, E. Ma, K. J. Hemker, H. Sheng, Y. Wang, and X. Cheng, Deformation twinning in nanocrystalline aluminum, *Science* **300**, 1275 (2003).
- [53] M. Gong, W. Wu, D. Xie, N. A. Richter, Q. Li, Y. Zhang, S. Xue, X. Zhang, and J. Wang, First-principles calculations for understanding microstructures and mechanical properties of Co-sputtered Al alloys, *Nanoscale* **13**, 14987 (2021).
- [54] Z. Fan, J. Li, Y. Yang, J. Wang, Q. Li, S. Xue, H. Wang, J. Lou, and X. Zhang, "Ductile" fracture of metallic glass nanolaminates, *Adv. Mater. Interfaces* **4**, 1700510 (2017).
- [55] Y. Wang, J. Ding, Z. Fan, L. Tian, M. Li, H. Lu, Y. Zhang, E. Ma, J. Li, and Z. Shan, Tension-compression asymmetry in amorphous silicon, *Nat. Mater.* **20**, 1371 (2021).
- [56] Y. B. Gerbig, C. A. Michaels, J. E. Bradby, B. Haberl, and R. F. Cook, *In situ* spectroscopic study of the plastic deformation of amorphous silicon under nonhydrostatic conditions induced by indentation, *Phys. Rev. B* **92**, 214110 (2015).
- [57] S. Plimpton, Fast parallel algorithms for short-range molecular dynamics, *J. Comput. Phys.* **117**, 1 (1995).
- [58] S. Starikov, I. Gordeev, Y. Lysogorskiy, L. Kolotova, and S. Makarov, Optimized interatomic potential for study of structure and phase transitions in Si-Au and Si-Al systems, *Comput. Mater. Sci.* **184**, 109891 (2020).
- [59] L. Zábanský, K. Bernátová, J. Dluhoš, R. Váňa, P. Souček, P. Vašina, and V. Buršíková, The effect of a taper angle on micro-compression testing of Mo-B-C coatings, *Mater* **13**, 3054 (2020).
- [60] F. Huiyang, A. Abraham, N. Chawla, and H. Jiang, Evaluation of micro-pillar compression tests for accurate determination of elastic-plastic constitutive relations, *J. Appl. Mech.* **79**, 061011 (2012).